JGR Oceans

RESEARCH ARTICLE
10.1029/2020JC016750

The Impact of Climate Change on Ocean Submesoscale Activity

K. J. Richards[1,2], D. B. Whitt[3,4], G. Brett[1], F. O. Bryan[3], K. Feloy[2], and M. C. Long[3]

[1]International Pacific Research Center, University of Hawai'i at Mānoa, Honolulu, HI, USA, [2]Department of Oceanography, University of Hawai'i at Mānoa, Honolulu, HI, USA, [3]National Center for Atmospheric Research, Boulder, CO, USA, [4]NASA Ames Research Center, Moffett Field, CA, USA

Abstract Global warming may modify submesoscale activity in the ocean through changes in the mixed layer depth (MLD) and lateral buoyancy gradients. As a case study we consider a region in the NE Atlantic under present and future climate conditions, using a time-slice method and global and nested regional ocean models. The high resolution regional model reproduces the strong seasonal cycle in submesoscale activity observed under present-day conditions. Focusing on the well-resolved winter months, in the future, with a reduction in the MLD, there is a substantial reduction in submesoscale activity, an associated decrease in kinetic energy (KE) at the mesoscale, and the vertical buoyancy flux induced by submesoscale activity is reduced by a factor of 2. When submesoscale activity is suppressed, by increasing the parameterized lateral mixing in the model, the climate change induces a larger reduction in winter MLDs while there is less of a change in KE at the mesoscale. A scaling for the vertical buoyancy flux proposed by (Fox-Kemper et al., 2008; doi:10.1175/2007JPO3792.1) based on the properties of mixed layer instability (MLI), is found to capture much of the seasonal and future changes to the flux in terms of regional averages as well as the spatial structure, although it over predicts the reduction in the flux in the winter months. The vertical buoyancy flux when the mixed layer is relatively shallow is significantly greater than that given by the scaling based on MLI, suggesting during these times other processes (besides MLI) may dominate submesoscale buoyancy fluxes.

Plain Language Summary The physical structure of the upper ocean is an important control on ocean-atmosphere exchange of momentum, heat, freshwater, and gases such as carbon dioxide. It also regulates the distribution of nutrients and their delivery to the sunlit upper ocean, thereby impacting biological production. Processes occurring at horizontal scales of 1–10 km (the so-called submesoscale) play an important role in structuring the upper ocean. This study considers how these processes may change under global warming. We find, associated with a warming of the upper ocean, a significant decrease in submesoscale activity and a reduction in the associated vertical flux of heat. Our results strongly suggest changes at these scales and their impact on the upper ocean need to be taken into account when assessing the impact of global warming.

Key Points:

- Submesoscale activity is substantially reduced under global warming
- A scaling for the vertical buoyancy flux based on mixed layer instability overestimates the reduction in the flux under global warming
- The reduction in mixed depth under global warming is reduced when submescale activity is included

Correspondence to:
K. J. Richards,
rkelvin@hawaii.edu

Citation:
Richards, K. J., Whitt, D. B., Brett, G., Bryan, F. O., Feloy, K., & Long, M. C. (2021). The impact of climate change on ocean submesoscale activity. *Journal of Geophysical Research: Oceans*, *126*, e2020JC016750. https://doi.org/10.1029/2020JC016750

Received 7 NOV 2020
Accepted 4 APR 2021

1. Introduction

The physical structure of the upper ocean is an important control on ocean-atmosphere exchange of momentum, heat, freshwater, and gases such as CO_2. It also regulates the distribution of nutrients and their delivery to the euphotic zone (the sunlit upper ocean), thereby impacting net primary productivity. Determining the mechanisms structuring upper ocean dynamics is critical to understanding how the physical climate system and biogeochemical cycles function. Moreover, we expect climate change to strongly impact these processes.

Important processes are associated with submesoscale motions, which have lateral scales of order 1–10 km and are characterized by sharp density gradients (fronts) and strong jets with large Rossby number. These dynamical features can induce very strong vertical motions (Capet, McWilliams, et al., 2008; Klein & Lapeyre, 2009; McWilliams, 2016) that impact the vertical flux of nutrients and biomass, which can both fuel and significantly damp primary production locally (Lévy et al., 2001, 2012, 2018; Mahadevan, 2016). A major source of the strong vertical motions at these scales is mixed layer baroclinic instabilities (Boccaletti et al., 2007; Fox-Kemper et al., 2008). In addition to the direct impacts of vertical motions on nutrient and bi-

omass fluxes, the eddy-driven overturning stream function associated with submesoscale motions can lead to a restratification of the mixed layer (Fox-Kemper et al., 2008) that can promote phytoplankton blooms by alleviating light limitation (Mahadevan et al., 2012; Taylor & Ferrari, 2011). From scaling arguments suggested by (Fox-Kemper et al., 2008) (hereafter FFH) the strength of the overturning scales as $H^2|\nabla_h b|/|f|$, where H is the mixed layer depth (MLD), $|\nabla_h b|$ is the cross-front horizontal buoyancy gradient, and f is the Coriolis parameter. (The buoyancy, $b = -g\rho/\rho_0$ where g is the acceleration due to gravity, ρ density, and ρ_0 a reference density.)

Because mixed layer instability (MLI) may be a dominant process controlling the energetics of submesoscales when mixed layers are sufficiently deep (Callies, Flierl, et al., 2016), a useful indicator for submesoscale activity is the conversion rate of available potential energy (APE). On theoretical grounds, the APE conversion rate scales as $H^2|\nabla_h b|^2/|f|$ (FFH). FFH test this scaling in an idealized flow regime while Capet, Campos, et al. (2008) and Mensa et al. (2013) show it also holds in more realistic model flows of the Argentinian Shelf and Gulf Stream regions, respectively, although Capet, McWilliams, et al. (2008) found the FFH scaling to underpredict the associated vertical buoyancy flux by a factor of 2–3. The dependence on H (the MLD) indicates the potential for strong seasonal modulation of submesoscale activity. Indeed, both Capet, Campos, et al. (2008) and Mensa et al. (2013) find that submesoscale activity peaks in winter months when the mixed layer is deep. The role of variations in lateral density gradients in the seasonal variation of submesoscale activity varies regionally: the strength of lateral density gradients peaks with the depth of the mixed layer in the model Argentinian Shelf (Capet, Campos, et al., 2008) while this relationship does not hold for the model Gulf Stream region (Mensa et al., 2013). Sasaki et al. (2014) also find a strong seasonality in submesoscale activity in a model of the North Pacific with it peaking in late winter when the mixed layer is at its deepest. Observational evidence of seasonality is growing. Callies et al. (2015) provide evidence based on in situ observations in the relatively energetic NW Atlantic of a strong enhancement of mixed layer submesoscale activity during winter months. Seasonality in submesoscale activity is also observed in the more quiescent parts of the North Pacific subtropical gyre (Ascani et al., 2013) and the NE Atlantic (Thompson et al., 2016).

Given this background, there is great potential for global warming to produce significant changes in ocean circulation dynamics at the submesoscale with unknown implications for the biogeochemistry and ecology of the upper ocean: in regions where there is an increase in the stratification of the near-surface ocean and a decrease in MLD there is expected to be a reduction in submesoscale activity. In a complex system such as the ocean, the degree to which this conjecture holds true, or how important the processes may be, is not obvious. Whether changes in lateral buoyancy gradients, brought about by changes to eddy stirring for instance, will enhance or suppress MLIs is unclear. Furthermore, there will certainly be regional dependencies. Indeed, the analysis of CMIP3 models by Capotondi et al. (2012) shows regional variation in the projected change in upper ocean stratification during the second half of the 21st century relative to the second half of the 20th century, with the largest changes in the tropics, the Arctic, the North Atlantic, and the northeast Pacific.

As a first step in evaluating the role of submesoscale processes in modulating the upper ocean response to climate change we present results from high-resolution nested regional simulations of the NE Atlantic. The simulation results are assessed in the context of extant theory for submesoscale MLI. The experimental design is described in Section 2. Results are presented in Section 3 with a focus on changes to horizontal wavenumber spectra and vertical buoyancy fluxes induced by global warming. Conclusions and closing discussion are given in Section 4.

2. Experimental Design

2.1. Modeling Approach

Integrating a submesoscale resolving global model over a full climate-change scenario would be computationally expensive. Instead, we use a "time slice" approach, which makes use of several models and observations to generate submesoscale permitting solutions in a particular region and a "time slice" of interest (e.g., present day, nominally year 2000, or future climate, nominally at 2100). First we describe the forcing that is used for the present-day and future climate cases. Then we describe the global mesoscale-resolving

model and run under present day and future forcing. Finally we describe the regional ocean model run at submesoscale-permitting resolution used to downscale the present-day and future conditions.

Surface forcing with synoptic variability but without confounding interannual variability is obtained using the standard bulk flux algorithms of the Community Earth System Model (CESM) and the Coordinated Ocean-Ice Reference Experiment normal-year atmosphere based on atmospheric reanalysis from 1958 to 2000 (Griffies et al., 2009; Large & Yeager, 2004; Small et al., 2015; Whitt, Nicholson, & Carranza, 2019). The normal-year atmosphere is modified to approximate the conditions in 2100 by adding the monthly anomaly (2100–2000) of each forcing field (shortwave radiation, wind, surface air temperature, etc.) from the ensemble-mean annual cycle in the CESM large ensemble (CESM-LE; Kay et al., 2015). The CESM-LE includes 42 simulations of the historical emissions scenario (1920–2005) and the high-emissions Representative Concentration Pathway 8.5 (2006–2100) that differ from each other because very small random perturbations ($\mathcal{O}(10^{-14})$ K) are introduced to air temperature fields in 1920 (Kay et al., 2015). The ensemble mean anomalies represent the forced response of the climate system, averaging out natural modes of variability.

First, two branches are made from February 1, 2021 of the control simulation of Whitt et al. (2019), which is a global nominal 0.1° resolution mesoscale-resolving configuration of the Parallel Ocean Program (POP2) (Smith et al., 2010) coupled to the Community Ice Code version 5 (Bailey et al., 2018) forced by the repeating normal-year atmosphere. The present-day branch is simply continued for 10 years without modifying the configuration. In the future-climate branch, the CESM-LE ensemble mean ocean temperature and salinity anomalies (2100–2000) are added to the initial condition and then integrated forward with the constructed "future-climate" normal-year atmospheric forcing.

Submesoscale-permitting regional ocean simulations are obtained via nesting a high-resolution regional model within the global 0.1° model. The present-day and future-climate regional ocean simulations are conducted with the Regional Ocean Modeling System (ROMS) (Haidvogel et al., 2008; Shchepetkin & McWilliams, 2005); these simulations are the focus of this study. ROMS was integrated on a nominally 0.01° (1.25 km) grid with 180 vertical sigma levels that are spaced using Equations 2.2 and 2.4 of Shchepetkin and McWilliams (2009) and the stretching parameters $\theta_s = 7$, $\theta_b = 2$, and $h_c = 250$ m. The resulting vertical resolution is about 1.3 m at the surface and about 7.5 m at 250 m depth, and 43% of the grid levels are above 250 m. Lateral dissipation is done through a biharmonic hyperviscosity and hyperdiffusion with coefficients 3.3×10^6 m^{4}s^{-1} and 3.7×10^5 m^{4}s^{-1}, respectively.

The bottom depth is based on ETOPO2 bathymetry (National Geophysical Data Center, NOAA, 2006), which is then limited to a range of 5,000–1,200 m and smoothed to mitigate numerical issues following Beckmann and Haidvogel (1993). The lateral boundary conditions are linearly interpolated from daily output of the analogous global 0.1° POP simulations using radiation and nudging constraints. Finally, ocean surface boundary layer dynamics are governed by the K-profile parameterization of Large et al. (1994) with parameters as in the public ROMS repository at myroms.org. A diurnal cycle in solar radiation is imposed using analytic functions such that the daily mean solar radiation matches the normal year, and solar radiation penetrates using Jerlov type IB parameters (Paulson & Simpson, 1977).

Two additional runs are performed at a nominal 4 km resolution, and vertical grid spacing twice that of the 1.25 km runs. The lateral mixing coefficients are increased to be in line with those used in the POP runs with the damping affecting scales with a wavelength less than a nominal 60 km. Specifically the biharmonic hyperviscosity and hyperdiffusion coefficients are set to 1.728×10^{10} m^{4}s^{-1} and 1.92×10^9 m^{4}s^{-1}, respectively. Submesoscale motions are suppressed although, as seen below, not entirely eliminated. These runs will be referred to as "high viscosity" runs and included to demonstrate the impact of reduced submesoscale activity.

Each regional simulation is integrated for 3.3 years; this duration is chosen based on analysis of the 0.1° POP runs, which suggests there is little to gain from further integration since the adjustment process to the initial condition shock in the future-climate scenario is relatively slow after 3 years. Output for the whole integration period includes snapshots of model variables every 5 days together with 12 h averages. To consider higher frequency variability, snapshots every 3 h were output for a 30-day period.

2.2. Study Region

For the study here we consider a region in the NE Atlantic between 41°–51°N and 26°–13°W, which covers a region of deep ocean from the Porcupine Seabight (in the NE) to the eastern flank of the mid-Atlantic Ridge near the Azores (in the SW). This region was chosen for a number of reasons. At the eastern edge of the North Atlantic subtropical gyre the mean flow is relatively weak and the mesoscale kinetic energy (KE) moderate, the depth of the mixed layer undergoes a large seasonal cycle (roughly 30–300 m depth) and there is an observed seasonal cycle in submesoscale activity (Thompson et al., 2016). In addition, it is a region where large changes in the winter MLD and stratification are projected to occur under global warming caused in part by a surface freshening from Arctic ice melt (cf. Capotondi et al., 2012).

The fastest growing MLI wavelength is estimated to be 2–3 km in summer and 10–12 km (4–6 km) in present-day (future) winter. This wavelength is estimated here by $L_{MLI} = \left(2\pi \mid \nabla_h b \mid H \,/\, f^2\right)\sqrt{(1 + Ri_b^B) \,/\, (5 \,/\, 2)}$ (Stone, 1966), where the balanced bulk Richardson number $Ri_b^B = \Delta b f^2 \,/\, (\mid \nabla_h b \mid^2 H)$, H is the MLD based on a change in density from the surface of $\Delta\rho = 0.03$ kgm^{-3} and $\Delta b = g\Delta\rho/\rho_0$; all of the variables in L_{MLI} are smoothed to mesoscales by applying a five-point square spatial smoother eight times (e.g., as in Capet, McWilliams, et al., 2008) to instantaneous snapshots (the filter damps the amplitude of a wave with wavelength of 30 km by approximately 60%).

We focus primarily on the wintertime, when submesoscales are strongest and their energetics is evidently closely linked to MLI, which is resolved in both the present and future simulations and exhibits a strong forced response to global warming in the North Atlantic (noting that the MLI in the summer may not be adequately resolved in our experiments).

3. Results

The runs of the regional model at 1.25 km resolution for the present-climate and future scenarios are labeled Run 2000 and Run 2100, respectively. The equivalent for the high viscosity runs are labeled Run 2000visc and Run 2100visc. A key feature of the upper ocean is the depth to which properties are mixed from the surface. Here the MLD is taken as the depth H at which the change in density from the surface equals $\Delta\rho = 0.03$ kgm^{-3}.

Snapshots of H taken at 00:00 UTC (23:00 local time) on February 15 are shown in Figure 1 for the various runs in the last year of integration. In the present-climate there is considerable variation in H across the domain, with the shallow layers toward the West impacted by the presence of fresher surface waters. There is a damping of the finer scales in the high viscosity run. The large variation in H is reflected in the broad spread of the probability distribution function (PDF) of layer depths with a reduction in the number of occurrences of deeper values in the higher resolution run (Run 2000) compared with the high viscosity run (Run 2000visc). In the future climate there is an overall reduction in H and a sharpening of the PDF of H, although it is notable that there is an increase in the number of occasions of shallower H in the high viscosity run (Run 2100visc).

The domain averaged MLD, $< H >$, and lateral buoyancy gradient $< |\nabla_h b| >$ within the mixed layer are shown as a function of time in Figure 2 for Runs 2000 and 2100. Day 0 here is February 1. In anticipation of examining the scaling for submesoscale activity following FFH, quantities have been spatially smoothed to the mesoscale (i.e., eight applications of a five-grid-point square window following Capet, McWilliams, et al., 2008). This does not affect $< H >$ but it does affect the quantiles of H. The depth of winter mixing is reduced in Run 2100 compared to Run 2000 (by a factor of more than 2 in the fourth winter of integration) with little change in the summer months.

For comparison the results for the high viscosity runs are shown. In the present-day climate the deepest winter time $< H >$ in Run 2000 is ∼20% less than in Run 2000visc, suggesting a restratification by the more active submesoscale activity in the former. There is little change between the runs in the summer. In contrast, comparing Runs 2100 and 2100visc, in the future climate state there is much less difference in $< H >$ throughout the year, with the notable exception of the fourth winter where $< H >$ is ∼20% deeper in Run

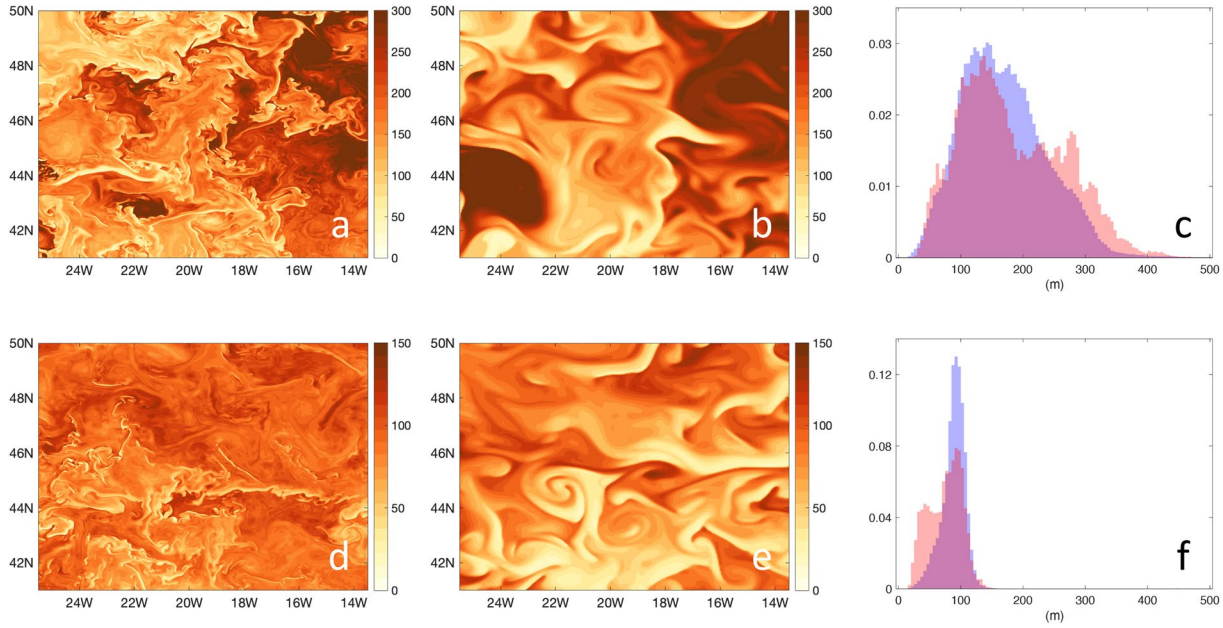

Figure 1. (a) Depth of the mixed layer, H, on February 15 in the present climate (Run 2000) over the ROMS domain. (b) The same as (a) but with high viscosity (Run 2000visc). (c) The PDF of the distribution of H in (a) and (b) (*blue* and *red*, respectively). (d)–(f) The same as (a)–(c) but for the future climate (Run 2100 and Run 2100visc). Units: m. Note the different y-axes in (c) and (f); the distribution of MLDs is more tightly clustered in the future climate (f).

2100 compared with the high viscosity run Run 2100visc (the snapshots shown in Figure 1 are from this winter).

There is a strong seasonal cycle in the mean lateral buoyancy gradient, $< |\nabla_h b| >$, with its magnitude anticorrelated with the MLD in both climate states, that is, the lateral buoyancy gradient is at a minimum during the deep winter mixing (Figure 2). The seasonality in the lateral buoyancy gradient is similar in both phase and amplitude to that found by Brannigan et al. (2015) who suggest frontogenesis strengthens gradients in the summer months while overturning instabilities, when the mixed layer is deep, weaken them in winter. There is notable interannual variability in both the mean MLD and lateral buoyancy gradient, the cause of which is not totally clear, although we note the long-term decrease with time of $< |\nabla_h b| >$ in Run

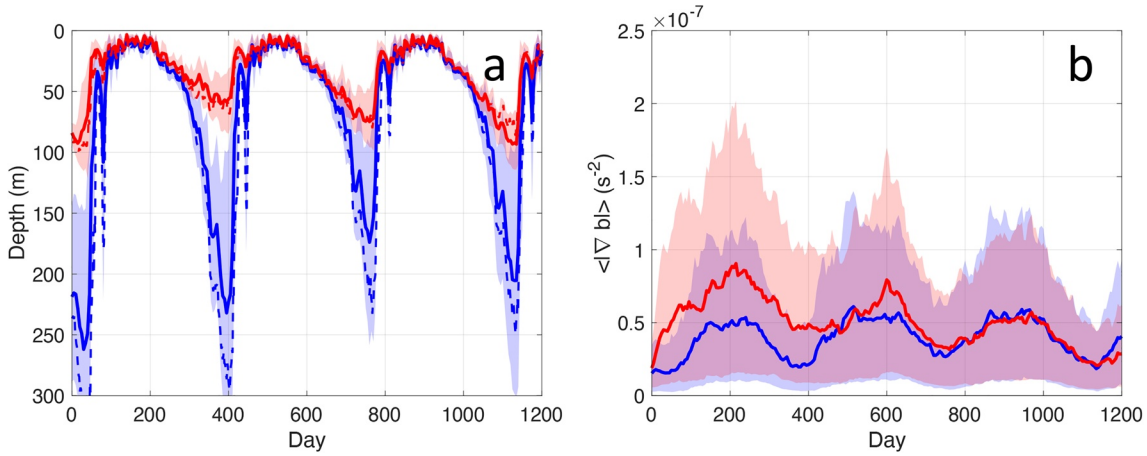

Figure 2. The areal average of (a) the mixed layer depth (based on the $\Delta\rho = 0.03$ kg/m^3 density threshold) and (b) the lateral buoyancy gradient as a function of time. Quantities are calculated from instantaneous snapshots of variables with a spatial filter applied to remove the smallest spatial scales (see text in Section 2.2): *solid blue* line Run 2000, *solid red* line Run 2100. The shading indicates the interval between the 0.1 and 0.9 quantiles. In (a), *dashed blue* line Run 2000visc; *dashed red* line Run 2100visc. Day 0 is February 1.

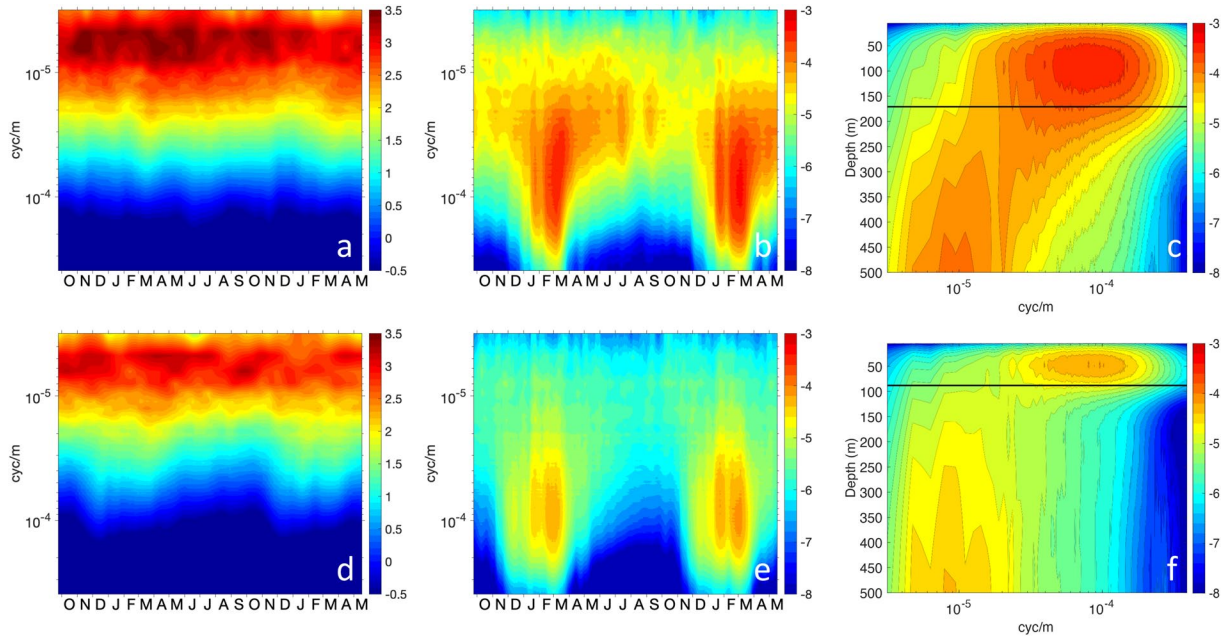

Figure 3. Radially integrated velocity horizontal wavenumber spectra. (a) and (b) $\log_{10}$ Horizontal and vertical kinetic energy power spectra for Run 2000, respectively, at a depth of 100 m as a function of wavenumber (cycles/m) and time (days 600–1200 with time indicated as month of the year). (c) $\log_{10}$ Vertical kinetic energy power spectrum on February 15, Year 4 for Run 2000 as a function and depth and wavenumber. (d)–(f) same as (a)–(c) but for Run 2100, with (d) and (e) at a depth of 50 m. Units m^2s^{-2} (cycles/m)$^{-1}$. Horizontal lines in (c) and (f) show the mean depth of the mixed layer. Fields are averaged over 36 h and a linear trend is removed from each column and row before the spectra are calculated.

2100 is associated with a reduction in the KE (which is not apparent in Run 2000). We will make use of this interannual variability when we come to consider the scaling of submesoscale activity in Section 3.2.

3.1. Spectra

Horizontal wavenumber spectra of velocity (Figure 3) reveal how the KE is decomposed by horizontal scale and, in particular, isolates the submesoscale activity from activity at other scales in both the 2000 and 2100 runs. Fields are averaged over 36 h and a linear trend is removed from each column and row before the spectra are calculated. The time series of horizontal and vertical KE spectra are at a depth of 100 m for Run 2000 (Figures 3a and 3b) and 50 m for Run 2100 (Figures 3d and 3e), the depths chosen to coincide with the depth of the peaks in vertical KE spectral energy (Figures 3c and 3f). There is a strong seasonal cycle in the vertical KE spectral energy, peaking in January to March at a horizontal wavelength centered on ~10 km and restricted to depths close to the MLD. There is a clear distinction between the vertical KE spectra in the mixed layer and the thermocline (Figures 3c and 3f): peak variance occurs at the submesoscales (O(10) km) within the mixed layer, whereas peak variance occurs at the mesoscales (O(100) km) in the thermocline below the mixed layer. Near the surface there is a seasonal cycle in the slope with respect to wavenumber at shorter scales (shallower in winter than summer, see Figure 4), with the seasonality dropping off with depth.

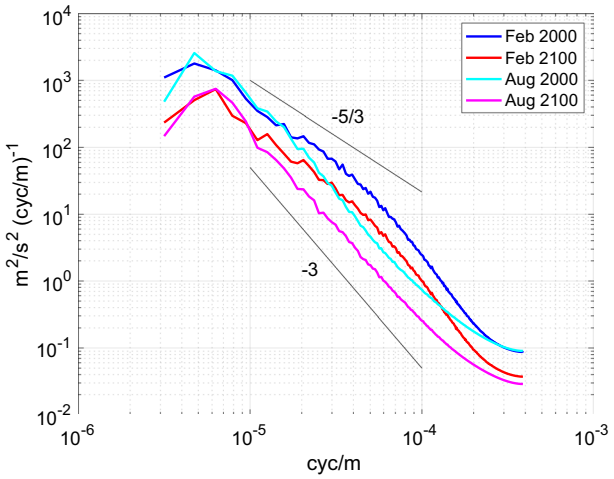

Figure 4. Horizontal wavenumber spectra of the horizontal kinetic energy at 20 m depth averaged over the months of August (Year 3) and February (Year 4) for Runs 2000 and 2100.

The horizontal KE spectral energy peaks at a wavelength of ~200 km. There is a reduction in energy at the mesoscale in the future run. Averaging the horizontal KE over wavenumber bands equivalent to 100–300 km

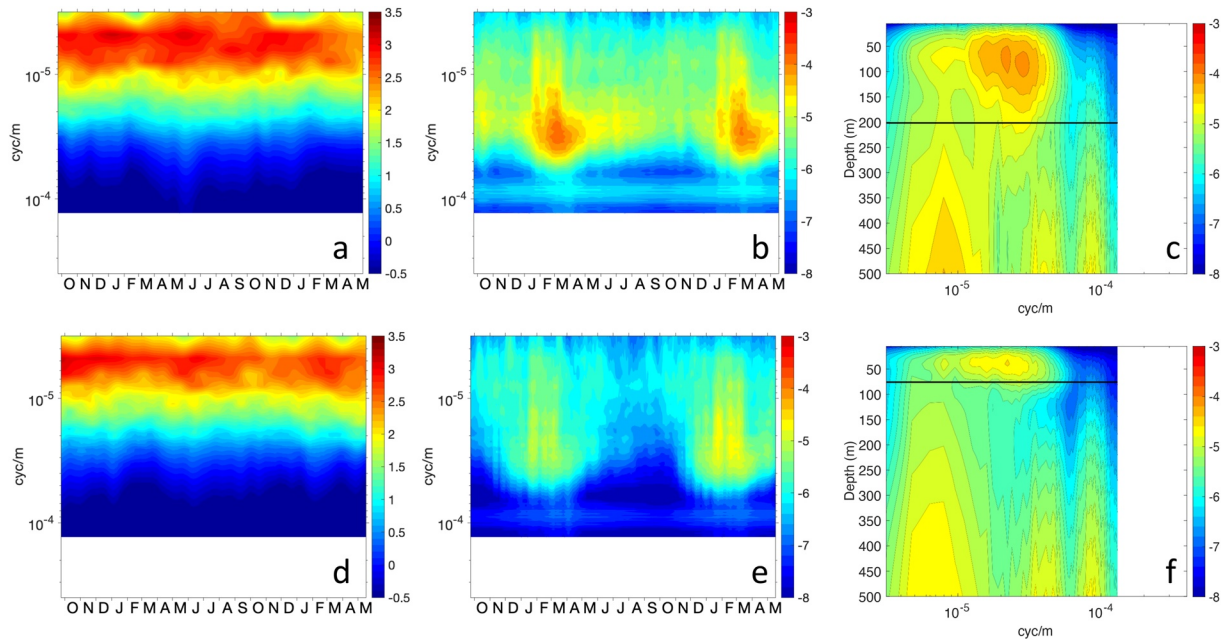

Figure 5. Same as Figure 3 but for Runs 2000visc and 2100visc.

wavelength and from the surface to 100m depth we find that the mesoscale KE reduces by 49% from 7.0 10^{-3} m^2s^{-2} in the 2000 run to 3.6 10^{-3} m^2s^{-2} in the 2100 run.

The spectra for the viscous runs 2000visc and 2100visc are shown in Figure 5. As expected there is a reduction in submesoscale activity, as seen in the vertical KE spectra, although it is not entirely eliminated. The submesoscale activity again peaks in the mixed layer and is reduced in amplitude in the future run, although at somewhat larger horizontal scale compared with the 2000 and 2100 runs. The average mesoscale KE is 2.4 × 10^{-3} m^2s^{-2} and 1.8 × 10^{-3} m^2s^{-2} in the 2000visc and 2100visc runs respectively, therefore reduced compared to Runs 2000 and 2100, but also a smaller reduction, 26%, in going from the present to future states. There is a similar reduction, 22%, in the KE of the surface flow in the region found in the present and future runs of the 0.1° POP model. (The elevated bands of power in the vertical KE spectra at high wavenumber, seen in Figures 5c and 5f, are presumed to come from the flow over the topography being inadequately resolved on the 4 km grid. Their presence does not appear to impinge unduly on the near-surface submesoscale).

The above spectral patterns are consistent with previous studies on submesoscale activity (e.g., Callies et al., 2015; Sasaki et al., 2014). Schubert et al. (2020) find a qualitatively similar but smaller ∼20% fractional reduction in the mesoscale KE when MLI are not included, or suppressed, in a model study centered on the Agulhas ring path. (Schubert et al. (2020) also find a seasonal variation in the length scale at which the upscale flux from submesoscale to mesoscale is a maximum, it being ∼15 km in winter, shifting to a larger scale in summer.) What we show here is that a substantial change in submesoscale activity can occur under environmental change such as global warming. There is a large reduction in that activity in the future-climate scenario (Run 2100) compared with the present (Run 2000) with a reduction in depth over which it occurs, associated with the reduced MLD.

We also note that there is a larger reduction in the mesoscale KE going from the present to future climate state (49% Runs 2000 and 2100, respectively) compared with when the submesoscale is suppressed (26% Runs 2000visc and 2100visc, respectively). Differences in the mesoscale KE between runs are consistent with changes in the upscale transfer of energy from the submesoscale to mesoscale: higher submesoscale activity leading to higher rates of transfer. What we do not see, however, is a noticeable seasonal variation in the mesoscale KE associated with the seasonal variation in submesoscale activity, as seen in other studies such as Dong et al. (2020).

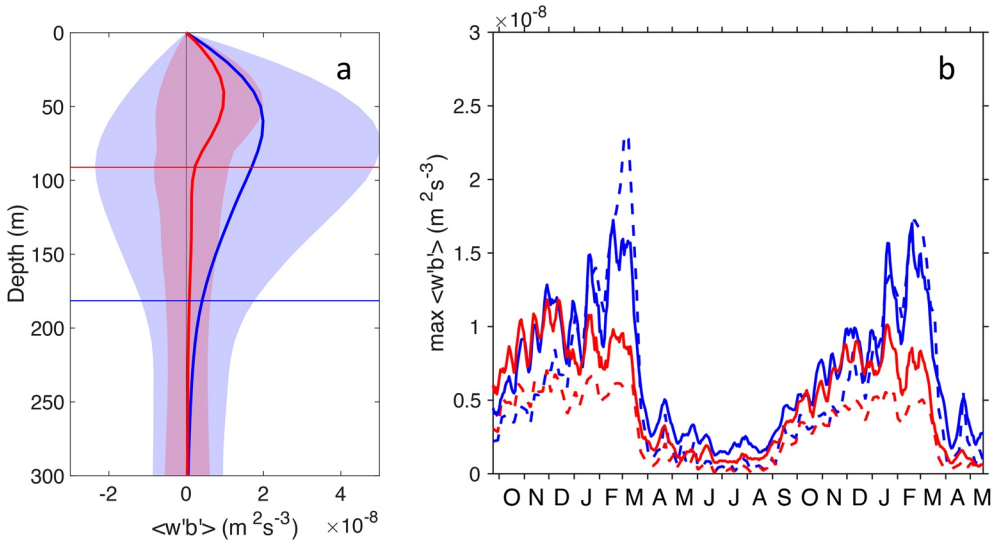

Figure 6. (a) The areal average vertical buoyancy flux $< w'b' >$ on February 15, Year 4 as a function of depth (the flux is calculated with 36-h averages of variables): *solid blue* line Run 2000, *solid red* line Run 2100. Horizontal lines show the mean depth of the mixed layer for each run. The shading indicates the interval between the 0.2 and 0.8 quantiles. (b) The maximum $< w'b' >$ within the mixed layer as a function of time for days 600–1200 (time is given as month of the year): *solid blue* line Run 2000, *solid red* line Run 2100. A 7-day running mean has been applied. Dashed lines are the FFH scaling for each run with the scaling coefficient $c = 0.08$.

3.2. Vertical Buoyancy Flux

An important property of submesoscale activity is the enhancement of the vertical buoyancy flux. The vertical profile of the areal average vertical buoyancy flux, $< w'b' >$, on February 15, Year 4 is shown in Figure 6a for Runs 2000 and 2100. Again, 36-h averages of w and b are used to compute the flux, prime indicates the areal mean and linear trend in both horizontal directions have been subtracted from the variable, and $< \cdot >$ the areal mean over the ROMS domain, excluding a 150 km strip around the boundary. An indication of the spatial variability is given in Figure 6a by the 0.2 and 0.8 quantile values (indicated by the shading).

Spatial variability of $w'b'$ on February 15, Year 4 is shown in Figures 7a and 7d for Runs 2000 and 2100 at a depth of 100 and 50 m, respectively (approximately the middle of the mean MLD at this time in each run). The regions of high flux tend to be spatially confined and filamentary in nature (particularly for Run 2100) with the density of such features significantly higher in Run 2000 compared with Run 2100. Positive fluxes tend to be higher in amplitude than negative fluxes (as reflected in the quantiles shown in Figure 6a) with the areal mean flux being 15.5×10^{-9} and 9.5×10^{-9} m^2s^{-3}, respectively. Figures 7b and 7e show the result of applying the spatial filter described above to smooth to the mesoscale for Runs 2000 and 2100, respectively. Although negative fluxes remain their contribution to the mean is much reduced.

The mean buoyancy flux, $< w'b' >$, peaks within the mixed layer (somewhat above the middle of the mean mixed layer for Run 2000), and is sharply reduced below the mean MLD, for both Runs 2000 and 2100 (Figure 6a). The vertical structure indicates a tendency for the density to decrease in the upper part of the mixed layer and increase in the lower, that is, a tendency, in the mean, for overturning within the mixed layer and restratification. The maximum $< w'b' >$ for Run 2000 is equivalent to a heat flux, Q_E, of ~40 Wm^{-2} (which is within the 20–100 W/m^2 range that is globally representative of midlatitudes in Su et al., 2018), where $Q_E = C_p\rho < w'b' >/(g\alpha_T)$ with C_p the specific heat and α_T the thermal expansion coefficient. The maximum buoyancy flux, and thus Q_E, is reduced by a factor of approximately 2 in Run 2100.

The maximum $< w'b' >$ within the mean mixed layer is shown in Figure 6b as a function of time. The time interval, days 600–1200, covers the winters of Years 3 and 4 (see Figure 2). There is a strong seasonal cycle. For both Runs 2000 and 2100 the max. $< w'b' >$ is relatively small in spring and summer (AMJJA), increasing through the fall and early winter (SOND). The max. $< w'b' >$ is somewhat smaller for Run 2100 compared to Run 2000 in spring and summer but the largest difference occurs in late winter (JFM). For Run

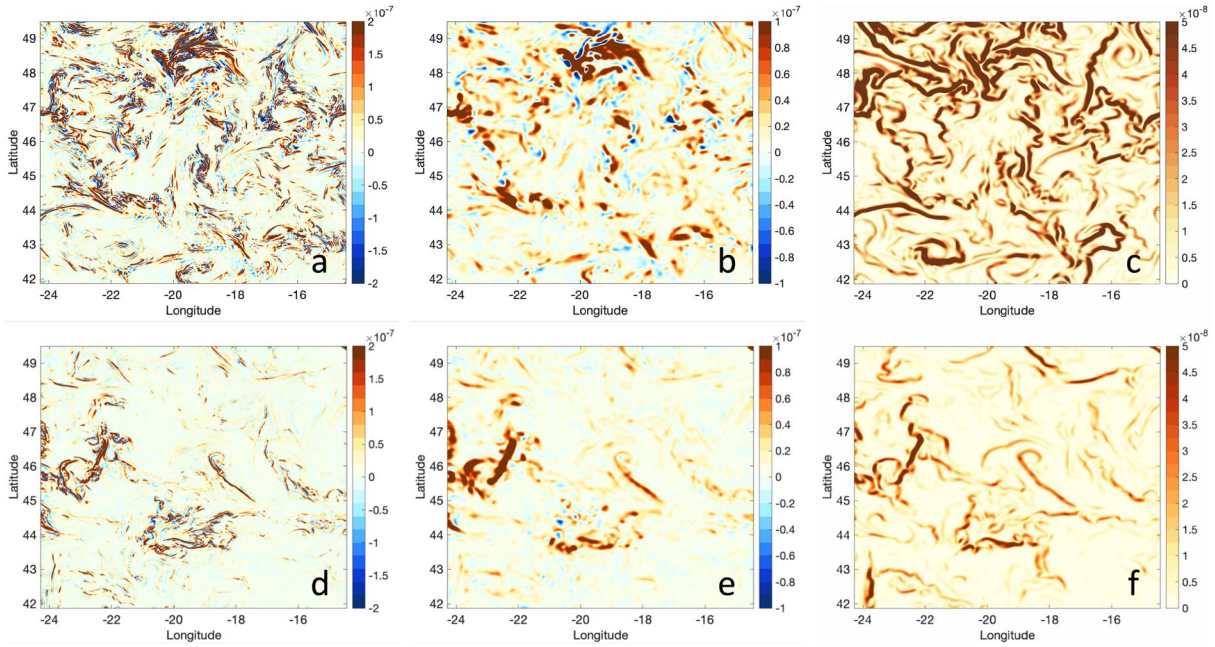

Figure 7. (a) Spatial variability of $w'b'$ for Run 2000 at a depth of 100 m on February 15, Year 4. (b) The same as (a) but with a spatial smoothing (smoothed to the mesoscale: see text) applied to the field. (c) The FFH scaling for Run 2000 on February 15, Year 4. (d)–(f) same as (a)–(c) but at a depth of 50 m for Run 2100. Units: m^2s^{-3} (note the color bars vary).

2000 the max. $< w'b' >$ continues to rise, peaking in February, while it is relatively constant for Run 2100, the difference in peak value being approximately a factor of 2.

Much of the variation in max. $< w'b' >$ is consistent with variations in the mean MLD (Figure 2a). The largest differences between Runs 2000 and 2100 occur in late winter (JFM) for both the buoyancy flux and mixed layer, when the latter is at its deepest. There are, however, inconsistencies. Despite the deeper MLD in Year 4 compared to Year 3 of Run 2000, the peak in the buoyancy flux is approximately the same (Figure 6b). In addition, the buoyancy flux in Run 2100 remains relatively flat during DJFM whereas the mixed layer is deepest in February (albeit at a shallower value than Run 2000).

For more insight into the factors controlling the buoyancy flux we turn to the scaling suggested by FFH. Using the properties of MLIs they suggest the buoyancy flux scales as $c < H^2|\nabla_h b|^2/|f| >$, where c is a scaling coefficient and H and $|\nabla_h b|$ are both smoothed to remove submesoscales before averaging (as in L_{MLI}). From idealized experiments of an unstable front they find that c lies in the range $c = 0.06$–0.08. The areal average of the FFH scaling is compared with the max. $< w'b' >$ in Figure 6b with $c = 0.08$ and quantities calculated as described above (i.e., eight applications of a five-grid-point square window).

The FFH scaling is somewhat sensitive to the level of smoothing. Reducing the smoothing scale by applying four applications of the five-grid-point square window to variables increases the areal mean FFH scaling by 40% (four applications of the smoother damps a wave with wavelength of 20 km by approximately 60%, whereas eight applications damps a wave with wavelength of 30 km by the same amount).

The areal mean of the FFH scaling captures well the seasonal behavior seen in max. $< w'b' >$ for both Runs 2000 and 2100 (Figure 6b), the former with a peak in late winter, the latter without. Even individual peaks on a monthly timescale are captured. A reduction in max. $< w'b' >$ between Runs 2000 and 2100 in late winter is also present in the FFH scaling, although with the same scaling coefficient, c, the FFH scaling over-predicts the reduction. FFH suggests a vertical structure function for the overturning stream function (μ(z) in their notation) that peaks in the middle of the mixed layer. The vertical position of max. $< w'b' >$ tends to be around 0.5 of the MLD in September decreasing to 0.3 and 0.4 of the MLD in February for Runs 2000 and 2100, respectively.

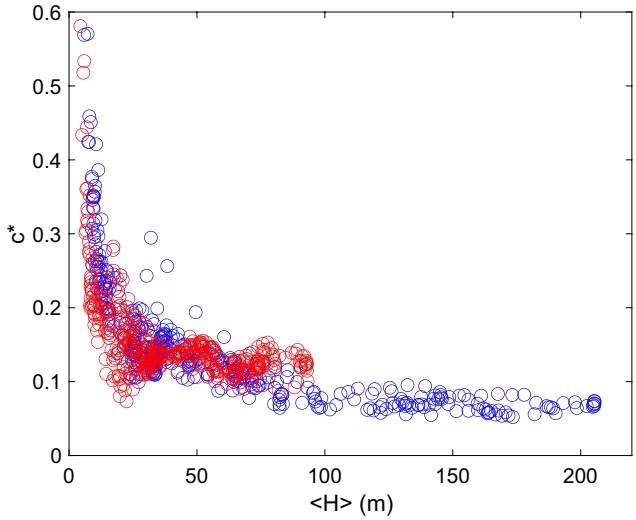

Figure 8. c^* ($= < w'b' > / < H^2|\nabla_h b|/|f| >$) Plotted as a function of the areal average mixed layer depth, $< H >$, for values from days 600 to 1200. *Blue* circles Run 2000. *Red* circles Run 2100.

The under-prediction of max. $< w'b' >$ by FFH when the areal mean MLD is relatively shallow may reflect the significance of other drivers of submesoscale vertical fluxes and restratification in shallow mixed layers (e.g., Long et al., 2012; Thomas, 2005; Whitt, Lévy, & Taylor, 2019; Whitt & Taylor, 2017). The ratio, c^*, of the areal means $< w'b' >$ and $< H^2|\nabla_h b|/|f| >$ plotted as a function of the areal averaged MLD, $< H >$, is shown in Figure 8 for values from days 600 to 1200 (the period shown in Figure 6b). Effectively, c^* is the scaling constant of the FFH scaling when fitted to the model results for a given value of $< H >$. For Run 2000 and large $< H >$, $c^* \simeq 0.08$, the value of c used in comparison of the FFH scaling and model results shown in Figure 6. For smaller values of $< H >$ there is an indication that the ratio (i.e., the scaling constant c) varies inversely with the areal mean MLD. For Run 2100 and $< H >$ between 50 and 100 m the ratio is approximately twice that of the asymptotic value for Run 2000. Similar to Run 2000, there is an increase in the ratio as $< H >$ decreases.

Again there is considerable spatial variability (see Figures 7c and 7f for Runs 2000 and 2100, respectively) with high values of the FFH scaling tracing out the areas of high amplitude buoyancy flux (Figures 7a and 7c, respectively), particularly evident in Run 2100. This is also true for the spatially smoothed buoyancy flux (Figures 7b and 7e), although we have not investigated the optimal smoothing for such a comparison. The comparison is somewhat better for the sparser structures seen in Run 2100. The areal mean of the FFH scaling (with $c = 0.08$) is 16.4×10^{-9} m^{2}s^{-3} and 4.8×10^{-9} m^{2}s^{-3} for Runs 2000 and 2100, respectively, the latter being approximately half the mean of $< w'b' >$ at 50 m. This is consistent with the results shown in Figure 8 (noting that max. $< w'b' >$ is used in the ratio c^* rather than the flux at a given depth).

The spatial variability in the FFH scaling is primarily caused by the spatial variability in $|\nabla_h b|$ rather than H. The variables contributing to the FFH scaling are compared in (Figure 9). The spatial variability of $|\nabla_h b|$ (Figure 9b) corresponds very well to that of the FFH scaling (Figure 9a), whereas there is less correspondence of the high values of H (Figure 9d) with the high values of the FFH scaling. Indeed there is a tendency for H to be shallower in regions where the scaling is high indicating either the choice of definition of the MLD picks out the frontal regions or the scaling is showing regions of restratification induced by submesoscale processes. Given the dominance of $|\nabla_h b|$, Figure 9b shows the FFH scaling with H^2 replaced by $< H >^2$, labeled FFH$_o$. The correspondence of FFH$_o$ with the original FFH scaling (Figure 9a) is very good. FFH$_o$ tends to overestimate FFH, again reflecting the tendency for H to be shallower in regions of high $|\nabla_h b|$.

Returning to the inconsistencies between variations of the buoyancy flux and the MLD alone, we see they can be resolved by including variations in the lateral buoyancy gradient with reference to the FFH scaling. The increase in the winter MLD, H, in Year 4 compared to Year 3 (Figure 2) is compensated by a decrease in the winter time $|\nabla_h b|$, resulting in little change in the buoyancy flux. In fact the FFH scaling over-compensates (Figure 6b). In Run 2100, the rate of decrease in $|\nabla_h b|$ in late winter is enough to compensate the rate of increase in H leading to the relatively flat variation with time in winter months.

Lastly, we have used 36 hourly averages of variables to compute the spectra and buoyancy flux. As shown by the modeling studies of Torres et al. (2018) and Su et al. (2020), however, there is considerable variability at higher frequencies. Observations also show submesoscale motions can have a relatively short time scale (Callies et al., 2020). Figure 10 compares the max. $< w'b' >$ within the mixed layer calculated using 3-h output compared to 36 hourly averages for a short (30 day) period at a time when the mixed layer is deep (see Figure 2). There is a strong diurnal signal as well as a near-inertial signal in the flux calculated with the high frequency output (established from a Fourier transform of the time series), on top of the lower frequency

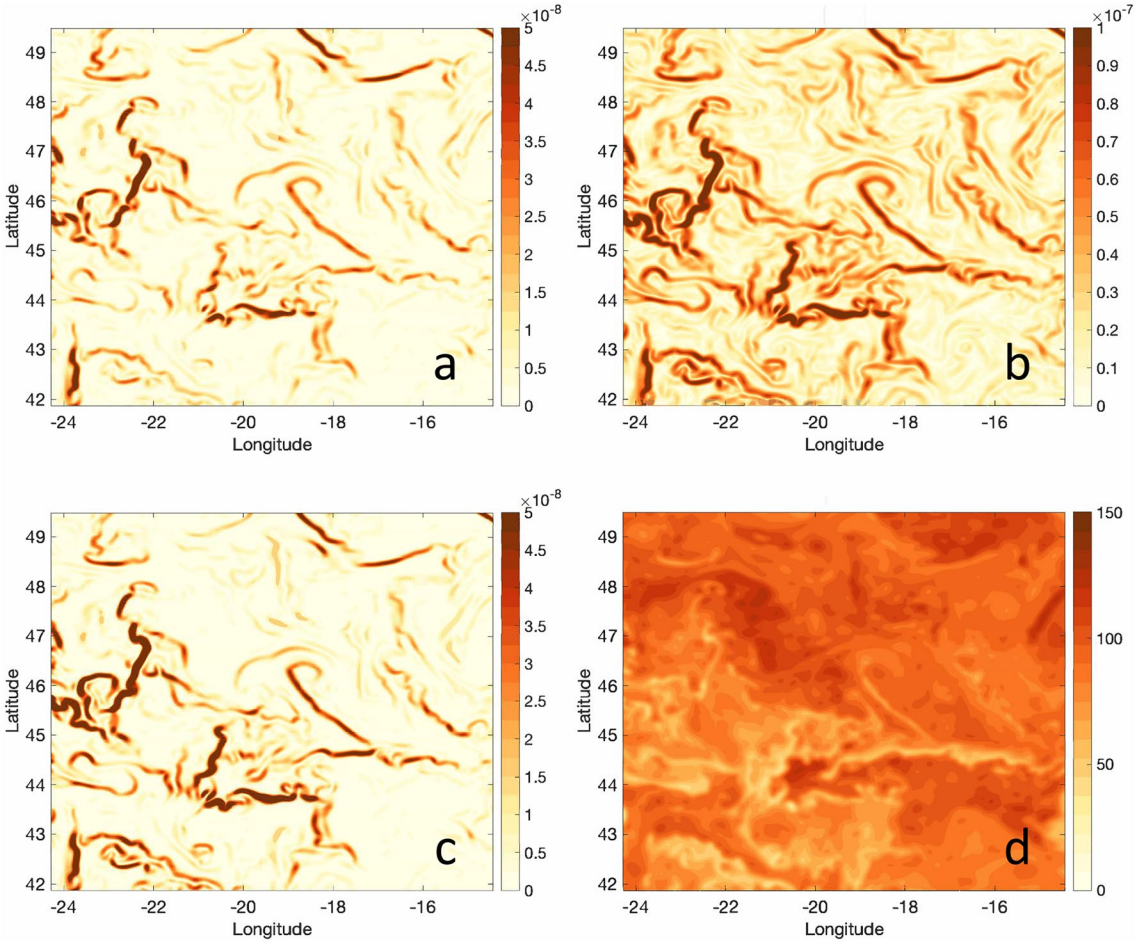

Figure 9. Contributions to the FFH scaling for Run 2100 on February 15, Year 4. (a) FFH scaling (m^2s^{-3}), (b) $|\nabla_h b|$ (s^{-2}), (c) FFH_o: FFH scaling with H^2 replaced by $< H >^2$, and (d) H (m).

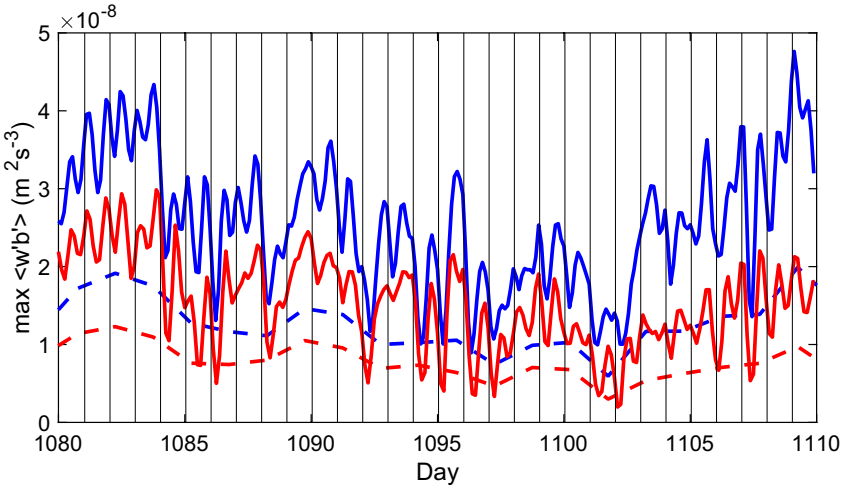

Figure 10. The maximum $< w'b' >$ within the mixed layer as a function of time comparing different temporal averaging of variables used in the flux calculation: solid lines high frequency (3 hourly) snapshots, dashed lines using 36-h averaged values of variables, *blue* lines Run 2000, *red* lines Run 2100. Local midnight indicated by *thin black* lines.

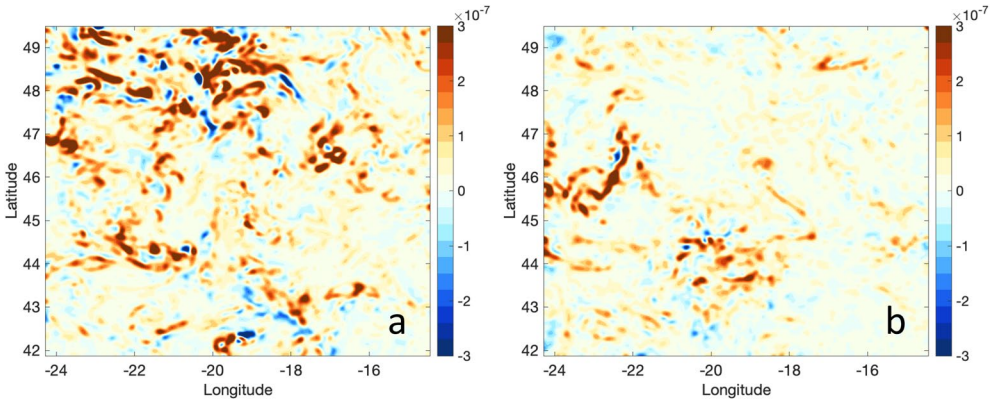

Figure 11. (a) Spatial variability of $w'b'$ calculated using snapshot values of w' and b' for Run 2000 at a depth of 100 m on 12:00 local time February 15, Year 4. A spatial smoothing (smoothed to the mesoscale: see text) has been applied to the field. (b) The same as (a) but at a depth of 50 m for Run 2100. Units: m^2s^{-3}.

variations found using the 36 hourly averages, that approximately doubles the flux averaged over the time period shown for both Runs 2000 and 2100.

The spatial variability of $w'b'$ on February 15, Year 4 using snapshot values of w' and b' is shown in Figures 11a and 11b for Runs 2000 and 2100 at a depth of 100 and 50 m, respectively. A spatial filter has been applied to smooth to the mesoscale. The spatial structure is similar to the result using 36-h averages and the FFH scaling (Figures 7b, 7c, 7e, and 7f, respectively). The areal mean is 4.0×10^{-8} and 2.1×10^{-8} m^2s^{-3}, respectively, a little over twice the values using 36-h averages.

To extend the period of comparison we have calculated the max. $< w'b' >$ from snapshots of w and b taken every 5 days throughout the integration period (see Figure 12). The snapshots are taken at 00:00 UTC (23:00 local time) when the flux tends to be relatively high (but not always: see Figure 10). In the winter months (deep mixed layer) the flux calculated from the 5-day snapshots tends to be greater than that calculated from 36-h averages by a factor ~2 for both Runs 2000 and 2100 (similar to that seen in Figure 10 for the high frequency snapshots). In the summer months there is less consistency. For Run 2100, there is no noticeable difference in the flux using the 5-day snapshots and 36-h averages, while for Run 2000 the 5-day snapshots do show periods when the flux is elevated.

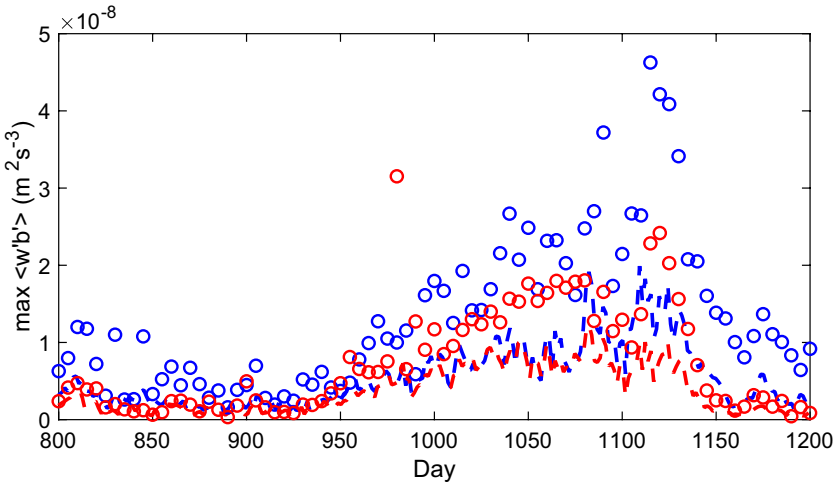

Figure 12. As Figure 10 but for snapshot values every 5 days (open circles) compared with 36-h averaged values (dashed lines).

4. Conclusions and Discussion

In the context of the experiments reported here we find the imposed climate change impacts submesoscale activity. Associated with a reduced MLD in a warmer climate there is a marked reduction in vertical motions at the submesoscale (Figure 3) together with a factor 2 decrease in the areal-mean vertical buoyancy flux in late winter (Figure 6). Changes to the lateral buoyancy gradient also play a role. We have seen that changes in the mean mesoscale lateral buoyancy gradient, $< |\nabla_h b| >$, in successive winters can counter changes to the mean MLD, although in the case considered (Years 3 and 4) the variation in $< |\nabla_h b| >$ was very similar in the present and future runs (Figure 2b). Longer simulations and examination of different regions are needed to establish the relative roles of future changes to MLD and lateral buoyancy gradients in affecting submesoscale activity.

To establish how the presence of submesoscale activity impacts the response to climate change, results are compared to runs with high lateral mixing coefficients to suppress (but not totally eliminate) submesoscale activity. In these runs where submesoscale activity was suppressed, climate change generated larger reductions in winter MLDs than in the submesoscale permitting integrations. The change at the mesoscale is also affected by the presence of submesoscale activity through changes to the nonlinear energy exchanges between mesoscales and submesoscales. The reduction in mesoscale KE going from the present to future climate states (Runs 2000 and 2100) at 49% is much greater than the reduction when the submesoscale is suppressed (Runs 2000visc and 2100visc) at 26%. The difference in these values comes primarily from the reduced mesoscale KE in Run 2000visc compared with Run 2000.

The scaling for the vertical buoyancy flux suggested by FFH, namely $cH^2|\nabla_h b|^2/|f|$, captures much of the seasonal and future changes to the areal mean flux (Figure 6b). The scaling offers a promising way forward in terms of parameterizing the impact of submesoscale activity. There are differences, however, and clearly the scaling does not capture all factors affecting changes to the vertical buoyancy flux, in particular when the MLD is relatively shallow or in the more stratified state in the future climate (see Figure 8). More numerical experimentation is needed to elucidate why these differences occur.

There are issues with regard to how well the grid resolution of the model runs resolves the submesoscale activity, as with all such studies (see, e.g., Brannigan et al., 2015), and in particular the changes to that activity under environmental change. Our conclusions need to be tested by establishing the sensitivity to the horizontal and vertical resolutions as well as the explicit diffusivities. Here we can report that additional runs with the coarser grid (~4 km) but with lower biharmonic lateral mixing coefficients, which lie between the high-viscosity and 1.25 km cases, show a similar factor 2 reduction in the vertical buoyancy fluxes in winter months as seen with the higher resolution ~1.25 km grid. With a grid spacing of ~1.25 km the model is not fully resolving the expected scales of MLI in the summer months. The results in the summer months need to be treated with caution, in particular with regard to changes, or lack thereof, from the present day to future climate states. We note, however, the vertical buoyancy fluxes when the mixed layer is relatively shallow are significantly greater than those given by the FFH scaling (if a constant scaling coefficient is used, Figure 8). Thus, other processes (besides MLI) that may be resolved on the 1.25 km grid may dominate submesoscale buoyancy fluxes during summer.

We stress the need to consider the lateral structure of the flow as well as areal means. Here we note the localized nature of the impact of submesoscale activity and the decrease in density of high flux regions within the domain going from the present to future climate states (see Figure 7). This localization will impact the biogeochemistry as well as the physics and needs to be considered when the submesoscale processes are parameterized. The dominance of the lateral buoyancy gradient in the FFH scaling at these small scales suggests that an effective estimate of the FFH scaling may be obtained from combining satellite measurements (to get an estimate of the lateral buoyancy gradient) and coarser in situ measurements (for MLD).

Lastly, we have noted the large impact of including diurnal and near-inertial variations in the calculation of the vertical buoyancy flux. There appears to be a consistent factor ~2 increase in winter months in the flux compared with the flux calculated with 36 hourly averaged values that filter out these high frequency variations for both the present-day and future climate states. There is less consistency in the summer months. Additional analysis and experimentation are needed to elucidate how quantities such as the vertical flux of buoyancy are impacted by the strength of the diurnal cycle and near-inertial motions and ocean state. The

theoretical framework presented in Dauhajre et al. (2017) and Dauhajre and McWilliams (2018) may help in the interpretation of numerical experiments.

Data Availability Statement

Datasets for this research are available at Richards et al. (2020a) and plotting scripts at Richards et al. (2020b).

Acknowledgments
This work is funded by the National Science Foundation (NSF) under grants OCE-1658550 and OCE-1658541. Discussions with Andrew Thompson on the experimental design and analysis of results are gratefully acknowledged. This material is based upon work supported by the National Center for Atmospheric Research, which is a major facility sponsored by the NSF under Cooperative Agreement No. 1852977. Computing and data storage resources, including the Cheyenne supercomputer (https://doi.org/10.5065/D6RX99HX), were provided by the Computational and Information Systems Laboratory (CISL) at NCAR. We thank all the scientists, software engineers, and administrators who contributed to the development of CESM. DBW also acknowledges support from the NSF, via OPP-1501993, NOAA, via NA18OAR4310408, and NASA, via 80NSSC19K1116.

References

Ascani, F., Richards, K. J., Firing, E., Grant, S., Johnson, K. S., Jia, Y., et al. (2013). Physical and biological controls of nitrate concentrations in the upper subtropical North Pacific Ocean. *Deep Sea Research Part II: Topical Studies in Oceanography*, *93*, 119–134. https://doi.org/10.1016/j.dsr2.2013.01.034

Bailey, D., DuVivier, A., Holland, M., Hunke, E., Lipscomb, B., Briegleb, B., et al. (2018). *CESM CICE5 Users Guide*.

Beckmann, A., & Haidvogel, D. B. (1993). Numerical simulation of flow around a tall isolated seamount. Part I: Problem formulation and model accuracy. *Journal of Physical Oceanography*, *23*(8), 1736–1753. https://doi.org/10.1175/1520-0485(1993)023<1736:nsofaa>2.0.co;2

Boccaletti, G., Ferrari, R., & Fox-Kemper, B. (2007). Mixed layer instabilities and restratification. *Journal of Physical Oceanography*, *37*(9), 2228–2250. https://doi.org/10.1175/JPO3101.1

Brannigan, L., Marshall, D. P., Naveira-Garabato, A., & George Nurser, A. J. (2015). The seasonal cycle of submesoscale flows. *Ocean Modelling*, *92*, 69–84. https://doi.org/10.1016/j.ocemod.2015.05.002

Callies, J., Barkan, R., & Garabato, A. N. (2020). Time scales of submesoscale flow inferred from a mooring array. *Journal of Physical Oceanography*, *50*(4), 1065–1086. https://doi.org/10.1175/JPO-D-19-0254.1

Callies, J., Ferrari, R., Klymak, J. M., & Gula, J. (2015). Seasonality in submesoscale turbulence. *Nature Communications*, *6*, 6862. https://doi.org/10.1038/ncomms7862

Callies, J., Flierl, G., Ferrari, R., & Fox-Kemper, B. (2016). The role of mixed-layer instabilities in submesoscale turbulence. *Journal of Fluid Mechanics*, *788*, 5–41. https://doi.org/10.1017/jfm.2015.700

Capet, X., Campos, E., & Paiva, A. (2008). Submesoscale activity over the Argentinian shelf. *Geophysical Research Letters*, *35*(15). https://doi.org/10.1029/2008gl034736

Capet, X., McWilliams, J. C., Molemaker, M. J., & Shchepetkin, A. F. (2008). Mesoscale to submesoscale transition in the California current system. Part I: Flow structure, eddy flux, and observational tests. *Journal of Physical Oceanography*, *38*, 29–43. https://doi.org/10.1175/2007JPO3671.1

Capotondi, A., Alexander, M. A., Bond, N. A., Curchitser, E. N., & Scott, J. D. (2012). Enhanced upper ocean stratification with climate change in the CMIP3 models. *Journal of Geophysical Research*, *117*, C04031. https://doi.org/10.1029/2011JC007409

Dauhajre, D. P., & McWilliams, J. C. (2018). Diurnal evolution of submesoscale front and filament circulations. *Journal of Physical Oceanography*, *48*, 2343–2361. https://doi.org/10.1175/jpo-d-18-0143.1

Dauhajre, D. P., McWilliams, J. C., & Uchiyama, Y. (2017). Submesoscale coherent structures on the continental shelf. *Journal of Physical Oceanography*, *47*, 2949–2976. https://doi.org/10.1175/jpo-d-16-0270.1

Dong, J., Fox-Kemper, B., Zhang, H., & Dong, C. (2020). The seasonality of submesoscale energy production, content, and cascade. *Geophysical Research Letters*, *47*. https://doi.org/10.1029/2020GL087388

Fox-Kemper, B., Ferrari, R., & Hallberg, R. (2008). Parameterization of mixed layer eddies. Part I: Theory and diagnosis. *Journal of Physical Oceanography*, *38*(6), 1145–1165. https://doi.org/10.1175/2007JPO3792.1

Griffies, S. M., Biastoch, A., Böning, C., Bryan, F., Danabasoglu, G., Chassignet, E. P., et al. (2009). Coordinated ocean-ice reference experiments (COREs). *Ocean Modelling*, *26*(1–2), 1–46. https://doi.org/10.1016/j.ocemod.2008.08.007

Haidvogel, D. B., Arango, H., Budgell, W. P., Cornuelle, B. D., Curchitser, E., Di Lorenzo, E., et al. (2008). Ocean forecasting in terrain-following coordinates: Formulation and skill assessment of the regional ocean modeling system. *Journal of Computational Physics*, *227*(7), 3595–3624. https://doi.org/10.1016/j.jcp.2007.06.016

Kay, J. E., Deser, C., Phillips, A., Mai, A., Hannay, C., Strand, G., et al. (2015). The community earth system model (CESM) large ensemble project: A community resource for studying climate change in the presence of internal climate variability. *Bulletin of the American Meteorological Society*, *96*(8), 1333–1349. https://doi.org/10.1175/bams-d-13-00255.1

Klein, P., & Lapeyre, G. (2009). The oceanic vertical pump induced by mesoscale and submesoscale turbulence. *Annual Review of Marine Science*, *1*(1), 351–375. https://doi.org/10.1146/annurev.marine.010908.163704

Large, W. G., McWilliams, J. C., & Doney, S. C. (1994). Oceanic vertical mixing: A review and a model with a nonlocal boundary layer parameterization. *Reviews of Geophysics*, *32*, 363–403. https://doi.org/10.1029/94rg01872

Large, W. G., & Yeager, S. G. (2004). *Diurnal to decadal global forcing for ocean and sea-ice models: The data sets and flux climatologies*. Colorado: National Center for Atomic Research. https://doi.org/10.5065/D6KK98Q6

Lévy, M., Ferrari, R., Franks, P. J. S., Martin, A. P., & Rivière, P. (2012). Bringing physics to life at the submesoscale. *Geophysical Research Letters*, *39*. https://doi.org/10.1029/2012GL052756

Lévy, M., Franks, P., & Smith, K. (2018). The role of submesoscale currents in structuring marine ecosystems. *Nature Communications*, *9*, 4758. https://doi.org/10.1038/s41467-018-07059-3

Lévy, M., Klein, P., & Treguier, A.-M. (2001). Impact of sub-mesoscale physics on production and subduction of phytoplankton in an oligotrophic regime. *Journal of Marine Research*, *59*(4), 535–565. https://doi.org/10.1357/002224001762842181

Long, M. C., Thomas, L. N., & Dunbar, R. B. (2012). Control of phytoplankton bloom inception in the Ross Sea, Antarctica, by Ekman restratification. *Global Biogeochemical Cycles*, *26*(1), GB1006. https://doi.org/10.1029/2010GB003982

Mahadevan, A. (2016). The impact of submesoscale physics on primary productivity of plankton. *Annual Review of Marine Science*, *8*, 161–184. https://doi.org/10.1146/annurev-marine-010814-015912

Mahadevan, A., D'Asaro, E., Lee, C., & Perry, M. J. (2012). Eddy-driven stratification initiates North Atlantic spring phytoplankton blooms. *Science*, *337*, 54–58. https://doi.org/10.1126/science.1218740

McWilliams, J. (2016). Submesoscale currents in the ocean. *Proceedings of the Royal Society A: Mathematical, Physical & Engineering Sciences*, *472*(2189). Royal Society, London. https://doi.org/10.1098/rspa.2016.0117

Mensa, J. A., Garraffo, Z., Griffa, A., Özgökmen, T. M., Haza, A., & Veneziani, M. (2013). Seasonality of the submesoscale dynamics in the Gulf Stream region. *Ocean Dynamics*, *63*, 923–941. https://doi.org/10.1007/s10236-013-0633-1

National Geophysical Data Center, NOAA. (2006). *2-Minute gridded global relief data (etopo2v2)*. https://doi.org/10.7289/V5J1012Q

Paulson, C. A., & Simpson, J. J. (1977). Irradiance measurements in the upper ocean. *Journal of Physical Oceanography*, *7*(6), 952–956. https://doi.org/10.1175/1520-0485(1977)007<0952:imituo>2.0.co;2

Richards, K., Whitt, D., & Brett, G. (2020a). *Climate change impact on submesoscale ROMS data (data set)*. http://doi.org/10.5281/zenodo.4615129

Richards, K., Whitt, D., & Brett, G. (2020b). *gjayb/submesoClimate: Initial release (Version v1.0)*. http://doi.org/10.5281/zenodo.4614207

Sasaki, H., Klein, P., Qiu, B., & Sasai, Y. (2014). Impact of oceanic-scale interactions on the seasonal modulation of ocean dynamics by the atmosphere. *Nature Communications*, *5*, 5636. https://doi.org/10.1038/ncomms6636

Schubert, R., Gula, J., Greatbatch, R. J., Baschek, B., & Biastoch, A. (2020). The submesoscale kinetic energy cascade: Mesoscale absorption of submesoscale mixed layer eddies and frontal downscale fluxes. *Journal of Physical Oceanography*, *50*, 2573–2589. https://doi.org/10.1175/jpo-d-19-0311.1

Shchepetkin, A. F., & McWilliams, J. C. (2005). The regional oceanic modeling system (ROMS): A split-explicit, free-surface, topography-following-coordinate oceanic model. *Ocean Modelling*, *9*, 347–404. https://doi.org/10.1016/j.ocemod.2004.08.002

Shchepetkin, A. F., & McWilliams, J. C. (2009). Correction and commentary for "Ocean forecasting in terrain-following coordinates: Formulation and skill assessment of the regional ocean modeling system" by Haidvogel et al., J. Comp. Phys. 227, pp. 3595-3624. *Journal of Computational Physics*, *228*(24), 8985–9000. https://doi.org/10.1016/j.jcp.2009.09.002

Small, R. J., Curchitser, E., Hedstrom, K., Kauffman, B., & Large, W. G. (2015). The Benguela upwelling system: Quantifying the sensitivity to resolution and coastal wind representation in a global climate model. *Journal of Climate*, *28*(23), 9409–9432. https://doi.org/10.1175/jcli-d-15-0192.1

Smith, R., Jones, P., Briegleb, B., Bryan, F., Danabasoglu, G., Dennis, J., et al. (2010). The parallel ocean program (POP) reference manual ocean component of the community climate system model (CCSM) and community earth system model (CESM). *Rep. LAUR-01853*, *141*, 1–140.

Stone, P. H. (1966). On non-geostrophic baroclinic stability. *Journal of the Atmospheric Sciences*, *23*(4), 390–400. https://doi.org/10.1175/1520-0469(1966)023<0390:ongbs>2.0.co;2

Su, Z., Torres, H., Klein, P., Thompson, A. F., Siegelman, L., Wang, J., et al. (2020). High-frequency submesoscale motions enhance the upward vertical heat transport in the global ocean. *Journal of Geophysical Research: Oceans*, *125*(9). https://doi.org/10.1029/2020JC016544

Su, Z., Wang, J., Klein, P., Thompson, A. F., & Menemenlis, D. (2018). Ocean submesoscales as a key component of the global heat budget. *Nature Communications*, *9*, 775. https://doi.org/10.1038/s41467-018-02983-w

Taylor, J. R., & Ferrari, R. (2011). Ocean fronts trigger high latitude phytoplankton blooms. *Geophysical Research Letters*, *38*, L23601. https://doi.org/10.1029/2011GL049312

Thomas, L. N. (2005). Destruction of potential vorticity by winds. *Journal of Physical Oceanography*, *35*(12), 2457–2466. https://doi.org/10.1175/jpo2830.1

Thompson, A. F., Lazar, A., Buckingham, C., Naveira Garabato, A. C., Damerell, G. M., & Heywood, K. J. (2016). Open-ocean submesoscale motions: A full seasonal cycle of mixed layer instabilities from gliders. *Journal of Physical Oceanography*, *46*, 1285–1307. https://doi.org/10.1175/jpo-d-15-0170.1

Torres, H. S., Klein, P., Menemenlis, D., Qiu, B., Su, Z., Wang, J., et al. (2018). Partitioning ocean motions into balanced motions and internal gravity waves: A modeling study in anticipation of future space missions. *Journal of Geophysical Research: Oceans*, *123*, 8084–8105. https://doi.org/10.1029/2018JC014438

Whitt, D. B., Lévy, M., & Taylor, J. R. (2019). Submesoscales enhance storm-driven vertical mixing of nutrients: Insights from a biogeochemical large eddy simulation. *Journal of Geophysical Research: Oceans*, *124*(11), 8140–8165. https://doi.org/10.1029/2019jc015370

Whitt, D. B., Nicholson, S. A., & Carranza, M. M. (2019). Global impacts of subseasonal (<60 day) wind variability on ocean surface stress, buoyancy flex, and mixed layer depth. *Journal of Geophysical Research: Oceans*, *124*(12), 8798–8831. https://doi.org/10.1029/2019JC015166

Whitt, D. B., & Taylor, J. R. (2017). Energetic submesoscales maintain strong mixed layer stratification during an autumn storm. *Journal of Physical Oceanography*, *47*(10), 2419–2427. https://doi.org/10.1175/jpo-d-17-0130.1